

# A multiscale finite element method for the dynamic analysis of surface-dominated nanomaterials

Harold S. Park\*,†

*Department of Mechanical Engineering, University of Colorado, Boulder, CO 80309, U.S.A.*

## SUMMARY

The purpose of this article is to present a multiscale finite element method that captures nanoscale surface stress effects on the dynamic mechanical behavior of nanomaterials. The method is based upon arguments from crystal elasticity, i.e. the Cauchy–Born rule, but significantly extends the capability of the standard Cauchy–Born rule by accounting for critical nanoscale surface stress effects, which are well known to have a significant effect on the mechanics of crystalline nanostructures. We present the governing equations of motion including surface stress effects, and demonstrate that the methodology is general and thus enables simulations of both metallic and semiconducting nanostructures. The numerical examples on elastic wave propagation and dynamic tensile and compressive loading show the ability of the proposed approach to capture surface stress effects on the dynamic behavior of both metallic and semiconducting nanowires, and demonstrate the advantages of the proposed approach in studying the deformation of nanostructures at strain rates and time scales that are inaccessible to classical molecular dynamics simulations. Copyright © 2010 John Wiley & Sons, Ltd.

Received 22 June 2009; Revised 21 December 2009; Accepted 4 January 2010

**KEY WORDS:** surface elasticity; Cauchy–Born; surface stress; nanoscale materials; finite elements; wave propagation

## 1. INTRODUCTION

Nanostructures such as nanowires [1] have been studied intensely in recent years due to their unique and often superior mechanical [1–3], electrical [4, 5] and optical [6–8] properties that arise because of their nanometer size scale. Because of these unique properties, nanowires will be utilized as structural and optical materials, bio-sensors, force and mass detectors, as circuitry and interconnects in future nanoscale devices, and as the basic building blocks of nanoelectromechanical systems (NEMS) [9–11].

---

\*Correspondence to: Harold S. Park, Department of Mechanical Engineering, University of Colorado, Boulder, CO 80309, U.S.A.

†E-mail: parkhs@bu.edu

Contract/grant sponsor: DARPA; contract/grant number: HR0011-08-1-0047

Contract/grant sponsor: National Science Foundation; contract/grant number: CMMI-0750395

In analyzing the mechanical behavior of nanowires, the key feature of interest is intrinsic surface stresses that arise due to the fact that surface atoms have fewer bonding neighbors, or are undercoordinated as compared with bulk atoms [12, 13]. Surface stresses have recently been found to cause phase transformations in gold nanowires [14], self-healing behavior in metal nanowires [15–17], and surface reorientations in thin metallic films and wires [18, 19]. The reduced bonding environment of surface atoms also alters the elastic properties of the surface atoms, which leads to non-bulk elastic [2, 3, 20–26] and inelastic [27–29] mechanical behavior and properties of both metallic and semiconducting nanowires [1]. Furthermore, the mechanical properties, i.e. Young's modulus of nanowires has been experimentally observed for both metals and semiconductors to deviate from the bulk value when the nanowire cross-sectional size decreases below about 100 nm [1, 3, 20, 24–26, 28].

From a computational perspective, the mechanical properties of nanostructures and nanowires have been studied using two distinct approaches. The first has been through classical molecular dynamics (MD) simulations [30], which have predicted that the elastic modulus of both metallic and semiconducting nanowires with cross-sections less than 10 nm may increase or decrease relative to that of the bulk elastic modulus depending on both the crystallographic and surface orientation [21, 23, 31–35]. However, scaling these results to larger nanowires while accounting for variations in size, surface and geometry has not been achieved due to computational expense, which limits not only the size of the nanowires that can be considered with MD simulations, but also the total physical time that the nanowires can be simulated for, as the time step in an MD simulation is typically about 1 fs, or  $10^{-15}$  s.

The second approach which has garnered significant interest within the past decade is the development of multiple scale methods to couple atomistics (typically MD) to continua (typically finite elements (FE) [36]). The underlying goal of these methods is to combine the salient features of the individual single-scale simulations, while limiting the less desirable features. For atomistic to continuum coupling, the salient features are the detailed resolution of atomic-scale physics that is possible using MD and the computational efficiency that is achievable through FE simulations; the challenge traditionally has been to mathematically combine these features into a single, coherent simulation. Toward this goal, a variety of different multiscale methods have been developed [37–39], which couple MD to FEM either concurrently [40–49], or hierarchically [50–55].

To motivate the current work, and to illustrate the shortcomings of existing multiscale computational methods for studying the mechanics of surface-dominated nanostructures, we show in Figure 1 a multiscale decomposition that is typically used in coupling atomistics to continua, or MD to FE. In Figure 1, we see that the problem of interest is crack propagation through the material. In the region of interest, the crack tip is explicitly modeled using an atomistic simulation (MD) such that accurate fracture characterization through the atomic-scale resolution of bond breaking is achieved. Surrounding the crack tip, and overlaying the atomistics is the continuum (FE) region; the purpose of the continuum region in the multiscale simulation is to enlarge the domain such that the stress  $\sigma_0$  that is used to load the crack tip can be applied to the far-field continuum boundaries.

As discussed previously, this philosophy of using atomistics to model critical physics of interest (i.e. cracks and defects), while using the continuum to extend the size of the domain has consistently been employed in the various quasistatic [38, 40–42, 50, 56] and dynamic [39, 43–49, 57] multiscale methods that have been recently proposed. However, the philosophy underlying the traditional multiscale decomposition shown in Figure 1 has led to two critical issues that cannot be circumvented without taking a different approach to multiscale modeling; these issues will be resolved or mitigated in the present work.

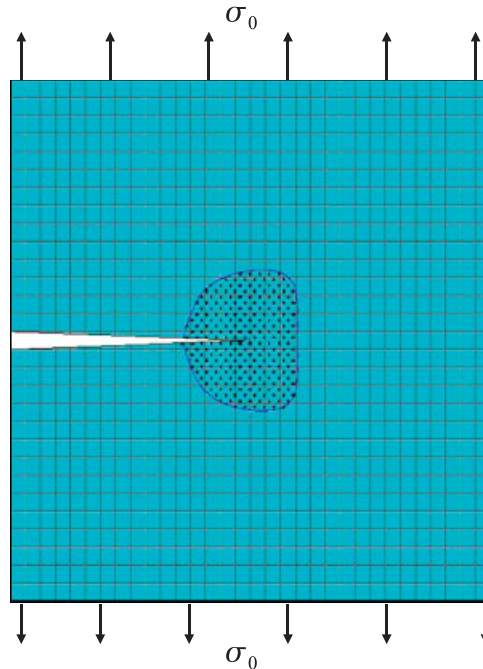


Figure 1. Schematic of a typical coupled atomistic–continuum multiscale decomposition, where the atomistics exists around the crack tip, and the finite element-discretized continuum exists everywhere.

First, the decomposition shown in Figure 1 indicates that because the continuum overlaps the atomistic region, the two simulations must be spatially as well as temporally coupled in some manner. We note that alternative decompositions exist [38, 40, 48] in which the continuum overlaps the atomistics only at the atomistic domain boundary. Regardless of the decomposition, to ensure stability of the atomistic region at the boundaries where it is coupled to the continuum, ghost, or pad atoms [38] are necessary; the effect of the ghost or pad atoms coupled with the surrounding continuum is to remove the effects of atomistic-free surfaces on the atomistic region. Therefore, multiscale methods formulated using this decomposition are unable to capture critical atomistic surface stress [13] and surface elastic effects [22], and therefore the size-dependent physical properties of nanomaterials.

The second key issue concerns the time scales that are accessible to the coupled multiscale atomistic–continuum simulation. While the decomposition in Figure 1 limits the extent of the atomistic domain to a small spatial regime, the atomistic region is still present, which is problematic because the time step for an atomistic simulation is on the order of  $10^{-15}$  s. In other words, while the multiscale decomposition in Figure 1 leads to a significant reduction in the number of atomistic equations of motion to be solved, the equations must still be integrated using a time step ( $10^{-15}$  s) that prevents the atomistic simulation from accessing physically meaningful time scales, i.e. time scales ranging from micro ( $10^{-6}$ ) seconds to milli ( $10^{-3}$ ) seconds, as accessing micro and millisecond time scales will be critical for analyzing the behavior and properties of novel NEMS [9].

Furthermore, this small MD time step leads to strain rates in MD simulations that are on the order of  $\dot{\epsilon} = 10^7\text{--}10^{10}\text{ s}^{-1}$ , which is about 10 orders of magnitude larger than is typically observed

experimentally. This strain rate differential may lead to unphysical or incorrect results in the MD simulations; for example, using novel time scale bridging techniques, Zhu *et al.* [58] studied the effects of strain rate and temperature on surface-driven dislocation nucleation for compressively loaded copper nanowires. In doing so, they found that the defect nucleation stress under compression is nearly 50% lower at room temperature and the strain rates of  $10^{-3} \text{ s}^{-1}$  as compared with the strain rates of  $10^8 \text{ s}^{-1}$  that are typically found in MD simulations.

Therefore, even though the FE mesh sizes in Figure 1 are typically two or three orders of magnitude larger than the atomic spacing, which implies that the FE equations of motion can be integrated forward in time using a time step that is two or three orders of magnitude larger than the atomistic time step, the MD time step is still the limiting factor on the overall time scales that are accessible to the coupled multiscale simulation due to the spatial and temporal coupling between the atomistics and continuum. Therefore, extending the time scales in multiscale simulations while still capturing the effects of essential nanoscale surface stress effects will require embedding the relevant atomic scale surface physics directly into the continuum simulation, thereby avoiding the explicit solution of the MD equations of motion.

The purpose of this work is to present and analyze a 3D dynamic formulation for the recently developed surface Cauchy–Born (SCB) model [53–55]. Understanding the effects of surface stresses on the dynamics of nanowires is critical for NEMS applications, where the nanowires will undergo oscillations at extremely high frequencies [9, 11]. The SCB model is unique as compared with previous FE discretizations of the linear surface elastic theory of Gurtin and Murdoch [59–62] in that it captures, within a non-linear continuum mechanics and FE framework, surface stress effects on the mechanical behavior and properties of nanomaterials. The SCB model [53] has previously been developed exclusively for quasistatic problems for both metallic [54] and semiconducting [55] nanostructures, and applied to problems analyzing surface stress effects on various aspects of the mechanical behavior and properties of both metallic [63, 64] and semiconducting [65, 66] nanowires.

Recently, a 1D formulation involving dynamics and the SCB model was formulated by Yun and Park [67]; in the present work, we significantly extend this formulation to 3D, and demonstrate its generality by using it to analyze the dynamic mechanical behavior for both metallic and semiconducting nanostructures while accounting for surface stress effects. We demonstrate that nanoscale surface stress effects can be captured within the present formulation, and discuss time step and strain rate improvements that can be gained using the FE-based SCB model as compared with classical MD simulations.

## 2. DYNAMIC PRINCIPLE OF VIRTUAL WORK INCLUDING SURFACE STRESS EFFECTS

We derive the dynamic finite element governing equations by beginning with a modified principle of virtual work as

$$\int_{\Omega_0} \delta \mathbf{u} \rho_0 \ddot{\mathbf{u}} \, d\Omega_0 = \int_{\Omega_0} \delta \mathbf{u} \frac{\partial \mathbf{P}_B}{\partial \mathbf{X}} \, d\Omega_0 + \int_{\Gamma_0} \delta \mathbf{u} \frac{\partial \mathbf{P}_S}{\partial \mathbf{X}} \, d\Gamma_0 + \int_{\Omega_0} \delta \mathbf{u} \rho_0 \mathbf{b} \, d\Omega_0, \quad (1)$$

where  $\mathbf{P}_B$  is the first bulk Piola–Kirchhoff stress,  $\mathbf{P}_S$  is the first surface Piola–Kirchhoff stress,  $\mathbf{b}$  is the body force and  $\delta \mathbf{u}$  is the virtual displacement. We note that the term involving the surface stress  $\mathbf{P}_S$  is integrated over an area rather than a volume due to the fact that the surface stress has units of force per length, rather than force per area as does the bulk stress  $\mathbf{P}_B$ ; this unit difference

was initially discussed by Park *et al.* [53], and is further discussed in Section 3 of the present work in relation to bulk and SCB theory.

The term on the left-hand side of (1) becomes the FE mass matrix upon discretization of the displacement field, while the last term on the right-hand side of (1) becomes the body force contribution to the external force. By integrating the first term on the right-hand side of (1) by parts, we obtain

$$\int_{\Omega_0} \delta \mathbf{u} \frac{\partial \mathbf{P}_B}{\partial \mathbf{X}} d\Omega_0 = \int_{\Omega_0} \frac{\partial}{\partial \mathbf{X}} (\delta \mathbf{u} \mathbf{P}_B) d\Omega_0 - \int_{\Omega_0} \frac{\partial \delta \mathbf{u}}{\partial \mathbf{X}} \mathbf{P}_B d\Omega_0. \tag{2}$$

The first term on the right-hand side of (2) becomes the applied traction, while the second term on the right-hand side of (2) becomes the internal force due to the bulk portion of the first Piola–Kirchoff stress  $\mathbf{P}_B$ .

By similarly integrating the surface term in the weak form (1) by parts, we obtain

$$\int_{\Gamma_0} \delta \mathbf{u} \frac{\partial \mathbf{P}_S}{\partial \mathbf{X}} d\Gamma_0 = \int_{\Gamma_0} \frac{\partial}{\partial \mathbf{X}} (\delta \mathbf{u} \mathbf{P}_S) d\Gamma_0 - \int_{\Gamma_0} \frac{\partial \delta \mathbf{u}}{\partial \mathbf{X}} \mathbf{P}_S d\Gamma_0. \tag{3}$$

The second term on the right-hand side of (3) becomes the internal force due to the surface Piola–Kirchoff stress  $\mathbf{P}_S$ , while the first term on the right-hand side of (3) becomes

$$\int_{\Gamma_0} \frac{\partial}{\partial \mathbf{X}} (\delta \mathbf{u} \mathbf{P}_S) d\Gamma_0 = (\delta \mathbf{u} \mathbf{n} \cdot \mathbf{P}_S)|_{dx}, \tag{4}$$

which is a 1D analog of the surface traction that results from the bulk Piola–Kirchoff stress in (2); we neglect this term in the present work by assuming that there are no such applied tractions. By combining (1)–(3) and making the FE approximation to the displacement field  $\mathbf{u}$ , we obtain the following semi-discrete FE equations of motion

$$\mathbf{M} \ddot{\mathbf{u}} = \mathbf{f}^{\text{ext}} - \mathbf{f}_B^{\text{int}} - \mathbf{f}_S^{\text{int}}, \tag{5}$$

where  $\mathbf{f}^{\text{ext}}$  combines the body force and any applied tractions,  $\mathbf{f}_B^{\text{int}}$  is the internal force due to the bulk Piola–Kirchoff stress  $\mathbf{P}_B$ , and  $\mathbf{f}_S^{\text{int}}$  is the internal force due to the surface Piola–Kirchoff stress  $\mathbf{P}_S$ . The semi-discrete equations of motion in (5) can be integrated in time using a standard explicit second-order central difference algorithm.

The issue that remains to be answered is how the bulk and surface Piola–Kirchoff stresses will be calculated. We describe this in the following section.

### 3. BULK AND SCB THEORY

In the present work, the bulk and surface stresses that are necessary to evaluate the dynamic FE momentum equation in (5) are obtained using the Cauchy–Born hypothesis. The bulk Cauchy–Born (BCB) model is a hierarchical multiscale assumption that enables the calculation of continuum stress and moduli directly from atomistic principles; the BCB model has successfully been applied to diverse crystal structures such as FCC metals [50], diamond cubic semiconductors such as silicon [68], and carbon nanotubes and graphene sheets [51, 52]. Because the BCB model does not consider surface effects, the SCB model was developed by Park *et al.* [53–55] such that the

strain energy density of a material would include contributions not only from the bulk, but also the material surfaces thus leading to the incorporation of atomistic-based surface stress effects into standard continuum stress measures.

Both the BCB and SCB models are finite deformation constitutive models that explicitly represent the stretching and rotation of bonds undergoing large deformation through continuum mechanics-based kinematic quantities such as the deformation gradient  $\mathbf{F}$ , or the stretch tensor  $\mathbf{C} = \mathbf{F}^T \mathbf{F}$ . Under deformations which can be represented as homogeneous over the unit cell scale, the approximation exactly reproduces the response of the corresponding, fully atomistic representation of the crystal. The necessity for the finite deformation kinematics gains credence through recent work that has indicated that surface stresses can cause *non-linearly elastic* compressive strains on the order of one percent or more in nanostructures [23, 54, 69].

For crystalline materials, the Cauchy–Born approximation is obtained through construction of a strain energy density function by considering the bonds in a representative volume of the crystal, and for a particular interatomic potential energy function  $U$ ; the discussion below represents a concise treatment of the more detailed exposition given in Park *et al.* [53]. For the case of a centrosymmetric crystal modeled using only pair interactions, the bulk strain energy density  $\Phi(\mathbf{C})$  is defined in terms of the interatomic potential  $U$  as [70]

$$\Phi(\mathbf{C}) = \frac{1}{2} \frac{1}{\Omega_0^a} \sum_{i=1}^{n_b} U(r^{(i)}(\mathbf{C})). \quad (6)$$

In (6),  $n_b$  is the total number of bonds to a representative bulk atom,  $\Omega_0^a$  is the representative atomic volume in the undeformed configuration and  $r^{(i)}$  is the deformed bond length which follows the relationship

$$r^{(i)} = \sqrt{\mathbf{R}_0^{(i)} \cdot \mathbf{C} \mathbf{R}_0^{(i)}}, \quad (7)$$

where  $\mathbf{R}_0$  is the undeformed bond vector, and the factor of  $\frac{1}{2}$  in (6) comes from splitting the energy of each bond.

The strain energy density (6) is exact in describing the change in energy per volume of a bulk atom in a corresponding defect-free atomistic system subject to homogeneous deformation. From (6), the bulk second Piola–Kirchhoff stress  $\mathbf{S}_B(\mathbf{C})$  is given by

$$\mathbf{S}_B(\mathbf{C}) = 2 \frac{\partial \Phi(\mathbf{C})}{\partial \mathbf{C}} = \frac{1}{\Omega_0^a} \sum_{i=1}^{n_b} \left( U'(r^{(i)}) \frac{\partial r^{(i)}}{\partial \mathbf{C}} \right), \quad (8)$$

where the first and second Piola–Kirchhoff stresses are related by the deformation gradient  $\mathbf{F}$  as

$$\mathbf{P}_B = \mathbf{S}_B \mathbf{F}^T. \quad (9)$$

For the SCB model, a surface strain energy density is needed; this surface strain energy density can be generally written as

$$\gamma(\mathbf{C}) = \frac{1}{2} \frac{1}{\Gamma_0^a} \sum_{i=1}^{n_{sl}} \sum_{j=1}^{n_{b_i}} U(r^{(j)}(\mathbf{C})), \quad (10)$$

where  $n_{sl}$  is the number of surface layers,  $n_{b_i}$  is the number of bonds for atoms in surface layer  $i$ ,  $\Gamma_0^a$  is the representative area of the entire surface layer cluster and the factor of  $\frac{1}{2}$  again comes due to splitting the energy of each bond.

Surface Cauchy Born: Bulk Cauchy-Born + Surface Modification

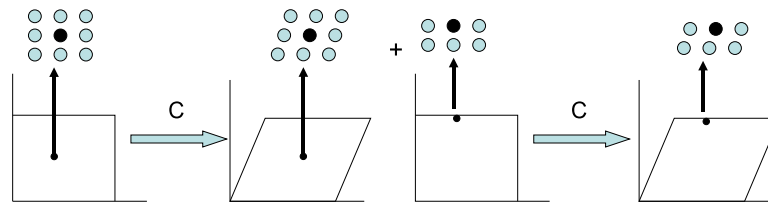


Figure 2. Illustration of difference between bulk and surface contributions to surface Cauchy–Born model.

We can immediately define the surface second Piola–Kirchoff stress  $S_S(\mathbf{C})$  resulting from the surface energy in (10) as

$$S_S(\mathbf{C}) = 2 \frac{\partial \gamma(\mathbf{C})}{\partial \mathbf{C}} = \frac{1}{\Gamma_0^a} \sum_{i=1}^{n_{sl}} \sum_{j=1}^{n_{bt}} \left( U'(r^{(j)}) \frac{\partial r^{(j)}}{\partial \mathbf{C}} \right). \quad (11)$$

Figure 2 summarizes the basic idea of the SCB model. For both bulk and surface components, the underlying atomistic potential energy is obtained by subjecting the bulk or surface unit cell to the continuum stretch tensor  $\mathbf{C}$ . Once the strain energy density of the deformed unit cell is known, the bulk stress can be calculated using (8), while the surface stress can be calculated using (11). Figure 2 demonstrates that both the bulk and surface unit cells are subject to the Cauchy–Born approximation, i.e. a homogeneous deformation of the unit cell.

We make two relevant comments regarding the definition of surface energy in (10) and surface stress in (11). The traditional thermodynamic definition of surface stress (see for example [13, 22]) is written as

$$\tau = \tau_0 + \mathbf{C}_0 \boldsymbol{\varepsilon}, \quad (12)$$

where  $\tau$  is the surface stress,  $\tau_0$  is the residual (strain-independent) portion of the surface stress, and  $\mathbf{C}_0 \boldsymbol{\varepsilon}$  is the surface-elastic (strain-dependent) part of the surface stress, where  $\mathbf{C}_0$  is the (constant) surface elastic stiffness. We note that the definition of surface stress in (12) is based upon linear elastic assumptions; the importance of finite deformation kinematics in modeling surface stress effects on the mechanical behavior and properties of metal nanowires was recently elucidated by Park and Klein [63], while the importance of utilizing finite deformation kinematics in studying the mechanical properties of silicon nanowires was recently demonstrated by Park [66].

The thermodynamic interpretation of both the surface stress  $\tau$  in (12) and that of the surface energy density  $\gamma(\mathbf{C})$  in (10) is that of an excess quantity, i.e. a measure of the difference as compared with the equivalent bulk quantity. The SCB surface energy density  $\gamma(\mathbf{C})$  in (10) differs from the conventional definition in that it does not represent the excess, or difference in energy density as compared with a typical bulk atom; instead, it represents the actual potential energy density of an atom lying at the surfaces of a nanostructure. We note that there has recently appeared multiple finite element formulations based upon the surface elastic formulation of Gurtin and Murdoch [59–62].

However, the definition of surface energy density utilized in the present work in (10) is extremely favorable for non-linear FE calculations. In particular, in an actual MD simulation, the force on a given atom, whether it lies within the bulk or on the surface, is obtained by differentiating its actual

potential energy, and not its excess energy, i.e. the difference of potential energy as compared with an ideal bulk atom. Therefore, the SCB definition of surface energy density in (10) leads directly to a surface stress, and thus an internal surface force  $\mathbf{f}_s^{\text{int}}$  in (5) that is similar in meaning to the force obtained on a surface atom in an MD calculation.

As previously discussed, the SCB model has been developed previously for both FCC metals using embedded atom (EAM) potentials [54, 63], and diamond cubic semiconductors such as silicon using Tersoff potentials [55, 65]. Both the bulk stress in (8) and surface stress in (11) can be obtained for either crystal structure and interatomic potential by deriving the appropriate energy densities  $\Phi(\mathbf{C})$  and  $\gamma(\mathbf{C})$ ; details on the EAM and Tersoff potentials as well as the SCB formulation for each can be found in [54, 55].

#### 4. NUMERICAL EXAMPLES

We perform numerical examples on both gold and silicon nanowires using both the BCB and SCB methods; both approaches are utilized to demonstrate the effects of including surface stress effects within the SCB formulation for dynamic simulations. In all cases, the bulk and surface energy densities for the gold nanowires were computed using the EAM potential developed by Foiles [71], while the bulk and surface energy densities for the silicon nanowires were computed using the T3 version of the Tersoff potential [72]. Both gold and silicon nanowires are assumed to have a  $\langle 100 \rangle$  axial orientation, with ideal, unreconstructed  $\{100\}$  transverse surfaces.

The non-linear, dynamic finite element simulations were performed using the Sandia-developed simulation code Tahoe [73]. A lumped mass matrix and standard explicit central-difference time integrator were used for all dynamic FE simulations; the explicit central-difference time integrator was also used to integrate the MD equations of motion.

We note that the dynamic behavior of nanomaterials including surface effects, for example wave propagation and uniaxial deformation, have rarely been studied within a continuum mechanics framework. Examples of the previous work include that of Wu and Dzenis [74], who studied wave propagation in nanofibers including surface effects. However, they only included surface tension  $\gamma$ , and did not consider the effects of either the residual (strain-independent) surface stress  $\tau_0$  or the surface elastic (strain-dependent) part of the surface stress  $\mathbf{C}_0\boldsymbol{\varepsilon}$ . Song *et al.* [75] studied wave propagation in nanowires including surface effects via a higher order continuum theory. However, they only considered the effects of the residual surface stress  $\tau_0$ . Neither formulation accounted for finite deformation effects due to surface stress, which has been shown to be critical in understanding the elastic properties of both metallic [63] and semiconducting nanowires [66].

##### 4.1. Surface stress effects on the dynamic tensile and compressive loading of gold and silicon nanowires

We first consider the dynamic tensile and compressive loading of both metallic and semiconducting nanowires. The geometry considered for both materials was a  $160 \times 10 \times 10$  nm nanowire, which was discretized with a regular mesh of 16 000 8-node hexahedral elements, leading to almost 20 000 FE nodes. The time step used for both the BCB and SCB simulations of the gold nanowire was 0.1 ps, while the time step for the BCB and SCB simulations of the silicon nanowire was 0.08 ps. Thus, to achieve a total simulation time of 500 ps, 5000 time steps were required for the gold nanowire, while 6250 time steps were required for the silicon nanowire.

For the gold nanowires, we also conducted classical MD simulations at zero temperature to compare against the SCB and BCB results. The precise geometry for the gold nanowires studied via MD was  $156.67\text{ nm} \times 9.792\text{ nm} \times 9.792\text{ nm}$  for a total of 923 185 atoms; the same EAM potential of Foiles [71] as was used for the BCB and SCB simulations was used in the MD simulations. The MD simulations were run for 125 000 steps with a time step of 0.004 ps, which is 25 times smaller than the FEM-based BCB and SCB time step; the total simulation time was 500 ps, the same as for the SCB calculations. We note that no surface reconstructions were observed in the MD simulations, thereby enabling a direct comparison between MD and SCB for the elastic behavior of the nanowires under applied tensile loading.

The nanowires were held fixed at the  $-x$  end, while the  $+x$  end was loaded using a force boundary condition where the applied force increased linearly from zero applied force on each FE node when  $t=0$  to a total applied (tensile or compressive) force per FE node of 0.8 nN at the completion of the simulation. A force boundary condition was used instead of a displacement or velocity boundary condition as those would lead to the same tensile or compressive strain in both the BCB and SCB nanowires; the force boundary condition does not impose that the strain is equal in both SCB and BCB nanowires, and therefore will enable us to delineate the effects of surface stresses on the tensile and compressive deformation of the nanowires.

The results for the gold nanowire are shown in Figure 3, while the results for the silicon nanowire are shown in Figure 4. Both figures plot the displacement time history for the center node on the  $+x$  face of the nanowires, and demonstrate the significant effect that surface stresses have on the dynamic uniaxial deformation of metallic and semiconducting nanowires.

For the tensile loaded gold nanowire in Figure 3(a), the BCB result, which neglects the effects of surface stresses, demonstrates a non-linear, but generally increasing displacement as a result of the applied tensile force; the total tensile strain in the BCB gold nanowire reaches almost 2% after 500 ps. However, the SCB result, which does account for surface stresses, is significantly different. One key difference is that for the first 250 ps of the simulation, the displacement of the tensile loaded end is actually negative, or in compression, despite the applied tensile force. The reason for this is because surface stresses on FCC metals are tensile [76], which means that the surface can lower its energy by contracting; the surface stresses thus oppose the applied tensile force in the gold nanowire. Previous studies on metal nanowires have clearly demonstrated that the tensile surface stresses at nanometer length scales are strong enough to cause significant compression in the nanowires leading to unique multifunctional nanomaterial behavior including phase transformations, shape memory, and pseudoelasticity [14–16]. The SCB results in Figure 3(a) thus demonstrate that it is only around  $t=240$  ps that the applied tensile force of 0.4 nN on each FE node of the gold nanowire is sufficiently large to counteract the effects of the surface stress, thus eventually leading to tensile expansion of the nanowire.

Figure 3(a) also demonstrates the accuracy of the SCB calculation as compared with the benchmark MD simulation for the tensile loaded gold nanowire. The MD simulation exhibits all of the same features as the SCB calculation, including the initial compressive deformation of the nanowire due to surface stresses, and subsequent tensile elongation once the applied tensile force exceeds the compressive surface stresses.

Figure 3(b) compares the BCB, SCB, and full MD results for compression of the gold nanowire. In the case of compression, the surface stresses induce the opposite effect as compared with tensile loaded gold nanowire, i.e. the tensile surface stresses augment the applied axial compression to cause the SCB and MD nanowires to exhibit a significantly larger compressive deformation for the same applied force as the BCB nanowire. Furthermore, we observe very good qualitative agreement

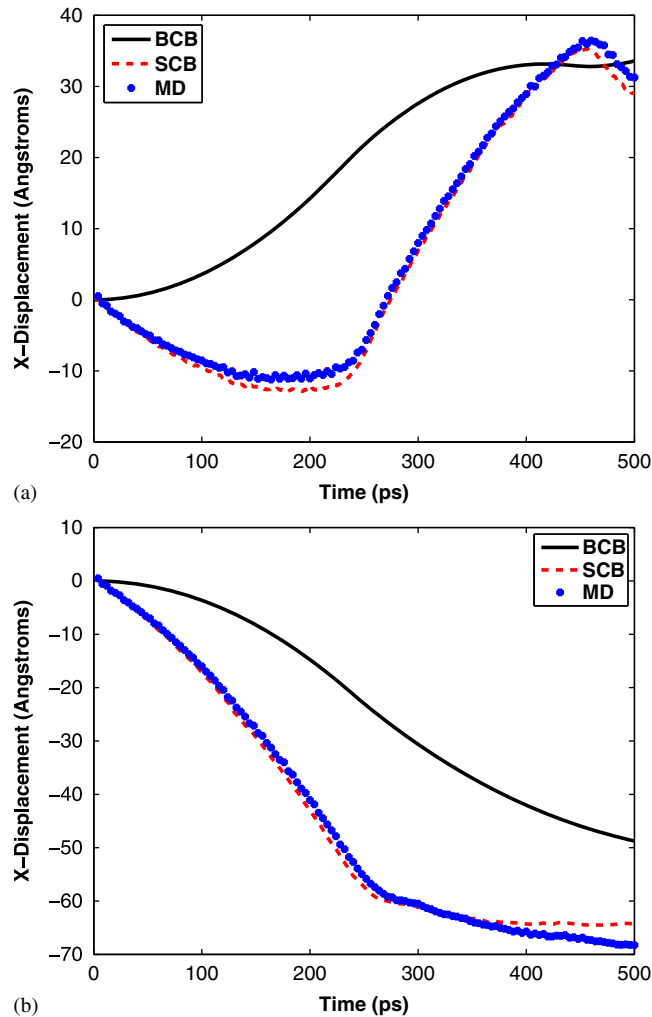


Figure 3. Displacement time history of a  $160 \times 10 \times 10$  nm gold nanowire loaded by (a) applied tensile force and (b) applied compressive force as computed using BCB and SCB models, and classical MD.

between the SCB and MD results, while emphasizing the reduction in computational cost obtained through using the SCB calculations both through a reduction in the number of degrees of freedom, as well as the significantly larger time integration step that can be used.

Similarly, the SCB results for the tensile loaded silicon nanowire in Figure 4(a) are significantly different from the BCB results, which again demonstrate a non-linear, but generally increasing displacement of the tensile loaded end. However, in contrast to the tensile loaded gold nanowire SCB results in Figure 3(a), the displacement of the silicon SCB nanowire is generally larger than that of the silicon BCB nanowire. The reason for this is because the surface stress for  $\{100\}$  silicon is compressive [77], which means that the surface can lower its energy by expanding. Thus, in the silicon SCB case, the surface stress actually enhances the applied tensile force, leading to the

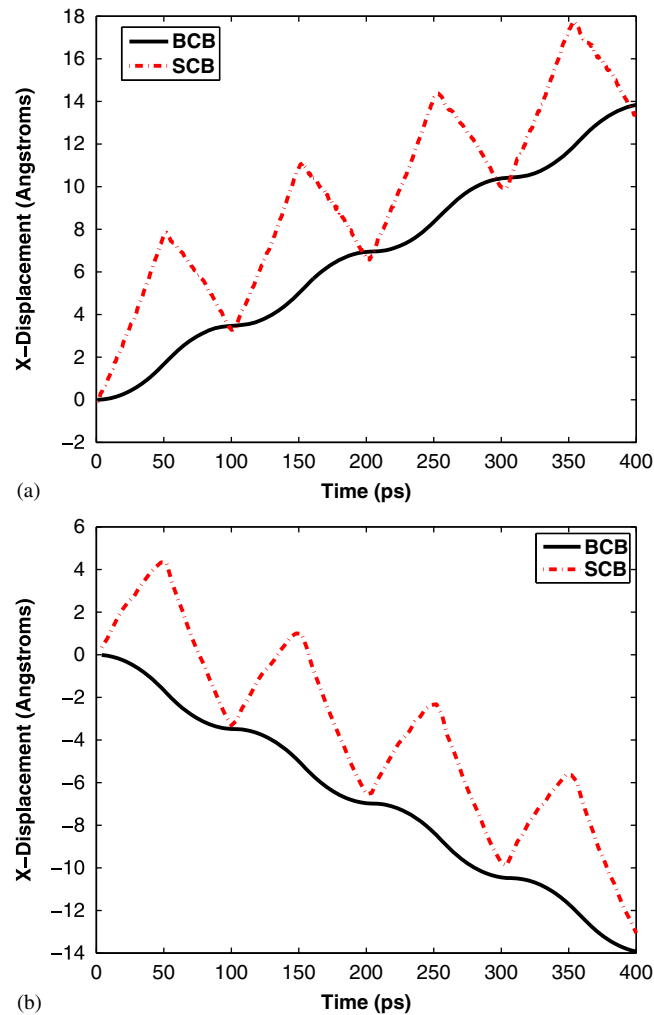


Figure 4. Displacement time history of a  $160 \times 10 \times 10$  nm silicon nanowire loaded by (a) an applied tensile force and (b) an applied compressive force as computed using BCB and SCB models.

larger displacements for the silicon SCB nanowire as compared with the BCB case where surface stress effects are ignored.

The results for the compressively loaded silicon nanowire are shown in Figure 4(b). There, it is observed that because the compressive surface stresses oppose the compressive axial force that is applied, the SCB nanowire deformation under compression is smaller than the BCB deformation. While a comparison with a benchmark MD simulation was not performed for the silicon nanowires, we note that the previous quasistatic calculations have found that the SCB model gives extremely accurate energy minimizing positions of nanowires due to surface stresses as compared with atomistic calculations [55, 65].

One of the distinct features for both the BCB and SCB silicon nanowire results in Figure 4 is the periodic oscillations, which are observed in both tension and compression, and are more distinct for the SCB results than the BCB results. The likely reason for this is due to the non-centrosymmetric nature of the silicon lattice; for example, as seen in the work of Park and Klein [55], fixed/free silicon nanowires show a non-uniform elongation strain due to the non-centrosymmetric nature of the silicon lattice. Therefore, the oscillations in the SCB results are expected to be greater than those in the BCB results due to the coupling between the undercoordinated nature of surface atoms and the non-centrosymmetric nature of both the bulk and surface atoms.

We also wish to make a few relevant remarks with regards to the dynamic simulations. First, we note that the time steps used above for the BCB and SCB calculations were very close to the maximum time step that is allowable numerically. We verified that just as in standard FE calculations, larger time steps can be used simply by increasing the element size. Second, it is worth mentioning that the stable time step for the BCB calculations is slightly larger than that of the SCB calculations. The likely reason is because in the SCB calculations the elements that lie on the surfaces are split, and receives contributions from both the bulk and surface energies; the splitting leads to slightly different material properties, i.e. stiffness and density due to the blending of bulk and surface properties, which causes the slight reduction in stable time step for the SCB calculations as compared with the BCB calculations.

We also comment on the time step in the FE simulation, and the reduction in strain rate as compared with classical MD. First, the time step in the FE simulation, which is about 0.1 ps, is about 100 times larger than the time step of 0.001 ps that is typically used in an MD simulation. Because of this, the FE-based SCB model can access significantly longer time scales than can MD simulations. Second, by approximating that the tensile deformation occurred uniformly for the gold and silicon nanowires, a strain rate of about  $\dot{\epsilon} = 3 \times 10^6 \text{ s}^{-1}$  is obtained for the FE-based SCB simulations. We note that by reducing the rate of applied loading, the strain rate can be reduced to something on the order of  $\dot{\epsilon} = 10^2$  or  $10^3 \text{ s}^{-1}$ , which while being larger than that obtained experimentally, is 4–6 orders of magnitude smaller than that which is possible in MD.

#### 4.2. Surface stress effects on flexural wave propagation in metal nanowires

The final numerical example considers surface stress effects on flexural wave propagation in gold nanowires. For this wave propagation example, the nanowires had square cross-sections of length 12 nm, while the nanowire length varied between 384 and 1152 nm depending upon the period of the input wave. The nanowires were discretized using a regular mesh of 8-node hexahedral elements, leading to FE mesh sizes that ranged from 32 000 to 170 000 elements.

In order to obtain the dispersion relationship, we follow the methodology described by Wang and Hu [78]. To do so, we applied sinusoidal transverse (flexural) displacements with a period of oscillation ranging from  $T = 10 - 100$  fs at one end of the nanowires, while the FE nodes at the other end of the nanowire were held fixed. Upon propagating a transverse wave through the nanowire, the propagation duration  $\Delta t$  of the wave from a point  $x_1$  to a point  $x_2$  along the nanowire can be written as

$$\Delta t = \frac{(t_{32} - t_{31}) + (t_{42} - t_{41}) + \dots + (t_{n2} - t_{n1})}{n - 2}, \quad (13)$$

where  $t_{32}$  is the time of the third peak of oscillation measured at  $x_2$ , and  $t_{31}$  is the time for the third peak of oscillation to reach  $x_1$ . In the present numerical examples,  $x_1$  corresponds to a point that is 6 nm from the end of the nanowire where the sinusoidal wave is input, while  $x_2$  corresponds

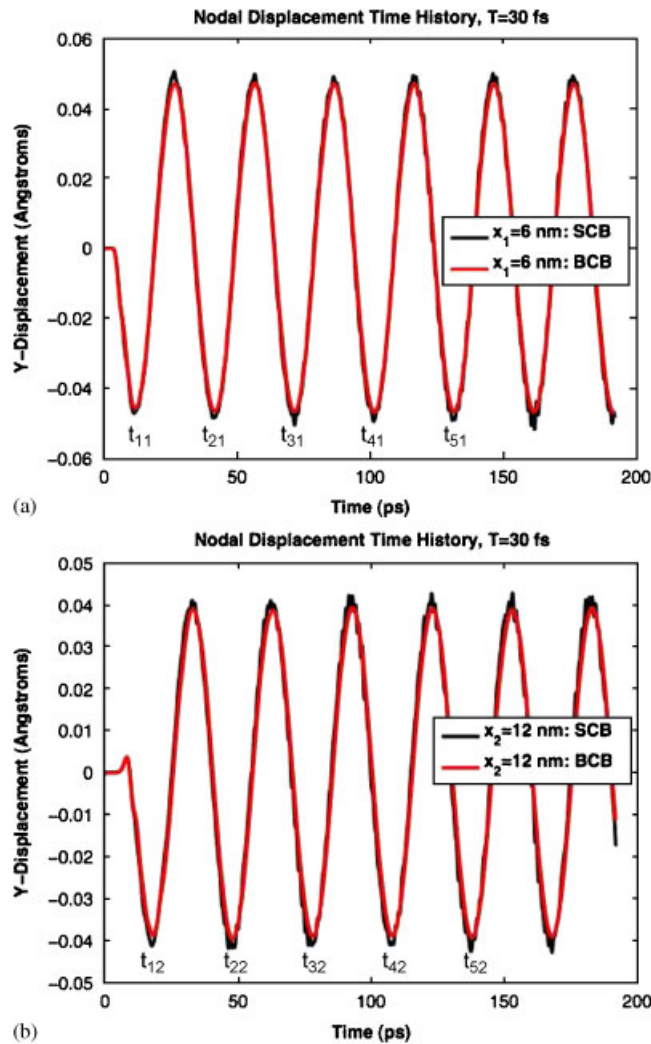


Figure 5. Wave propagation history at different sections along the gold nanowire length for input sinusoidal flexural wave of period  $T = 30$  ps for both SCB and BCB models.

to a point that is 12 nm from the end of the nanowire where the sinusoidal wave is input. We show in Figure 5 the displacement time history at points  $x_1$  and  $x_2$  for the input longitudinal wave of period  $T = 30$  fs; the time for different peaks of oscillation ( $t_{31}, t_{32}$ , etc.) that are needed to evaluate the propagation duration  $\Delta t$  are labeled for clarity.

Once the propagation duration  $\Delta t$  is known, the phase velocity  $c$  and the wave number  $k$ , which are required to calculate the dispersion relationship, can be found as

$$c = \frac{x_2 - x_1}{\Delta t}, \tag{14}$$

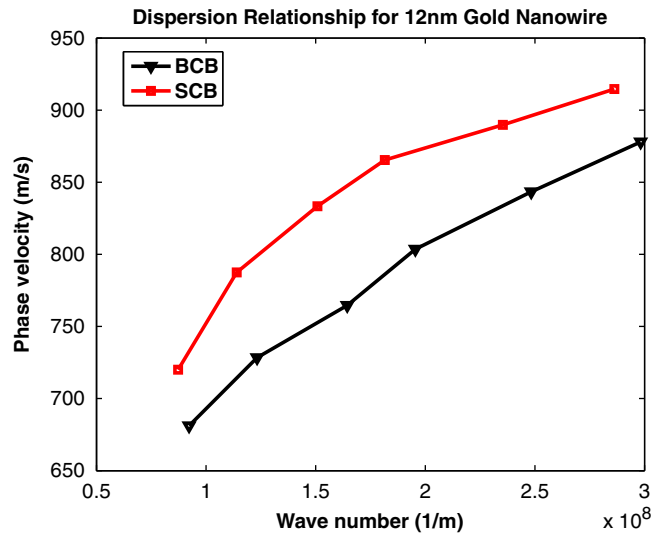


Figure 6. Dispersion relationship for a 12 nm square cross-section gold nanowire.

and

$$k = \frac{2\pi}{\lambda} = \frac{\omega T}{\lambda} = \frac{\omega}{c}, \quad (15)$$

where the angular frequency  $\omega$  is related to the period  $T$  by the relationship

$$\omega = \frac{2\pi}{T}. \quad (16)$$

The dispersion relationship for the 12 nm square cross-section gold nanowire is shown in Figure 6. As can be observed, both the BCB and SCB results demonstrate an increase in phase velocity with an increase in wave number; furthermore, the wave speeds in the SCB simulation are always greater than those in the BCB model. The reason for this is because the gold nanowires are held in a position in which the nanowires are under tension. In other words, due to one end being fixed while the other end is subjected to the input sinusoidal wave, the gold nanowires are unable to contract to relieve the tensile surface stresses, and thus naturally exist in a state of tension, thus leading to enhanced flexural wave speeds.

## 5. CONCLUSIONS

In conclusion, we have presented a dynamic finite element formulation which accounts for atomistically based surface stress effects on the mechanical response of nanomaterials. The finite element formulation is inherently multiscale through the usage of the Cauchy–Born hypothesis to obtain the constitutive response for both the bulk and surfaces of the nanostructure directly from underlying atomistic principles. The presented approach offers distinct computational advantages as compared with classical MD, including a time step that is about two orders of magnitude larger than that

used in atomistics, which enables both the simulation of strain rates ( $\dot{\epsilon} = 10^2 - 10^6 \text{ s}^{-1}$ ) that are significantly lower than those attainable in MD simulations, and thus are closer to those that are attainable experimentally, and also the attainment of time scales (i.e. micro and milliseconds) that are relevant for the study and analysis of NEMS.

The numerical examples of dynamic tension and compression of metallic and semiconducting nanowires, as well as flexural wave propagation in metal nanowires demonstrated the significant effect that surface stresses have on the dynamic mechanical behavior and response of both metallic and semiconducting nanostructures. Furthermore, the numerical examples quantified the advantages of the dynamic SCB model, i.e. accuracy as compared with fully atomistic calculations coupled with a significant reduction in computational expense.

#### ACKNOWLEDGEMENTS

HSP acknowledges the support of DARPA through grant HR0011-08-1-0047. The author notes that the content of this article does not necessarily reflect the position or the policy of the government, and that no official government endorsement of the results should be inferred. HSP also acknowledges support of the NSF through grant number CMMI-0750395.

#### REFERENCES

1. Park HS, Cai W, Espinosa HD, Huang H. Mechanics of crystalline nanowires. *MRS Bulletin* 2009; **34**(3):178–183.
2. Wong EW, Sheehan PE, Lieber CM. Nanobeam mechanics: elasticity, strength, and toughness of nanorods and nanotubes. *Science* 1997; **277**:1971–1975.
3. Cuenot S, Frétiigny C, Demoustier-Champagne S, Nysten B. Surface tension effect on the mechanical properties of nanomaterials measured by atomic force microscopy. *Physical Review B* 2004; **69**:165410.
4. Wiley BJ, Wang Z, Wei J, Yin Y, Cobden DH, Xia Y. Synthesis and electrical characterization of silver nanobeams. *Nano Letters* 2006; **6**(10):2273–2278.
5. Ohnishi H, Kondo Y, Takayanagi K. Quantized conductance through individual rows of suspended gold atoms. *Nature* 1998; **395**:780–783.
6. Canham LT. Silicon quantum wire array fabricated by electrochemical and chemical dissolution of wafers. *Applied Physics Letters* 1990; **57**(10):1046–1048.
7. Barnes WL, Dereux A, Ebbeson TW. Surface plasmon subwavelength optics. *Nature* 2003; **424**:824–830.
8. Xia Y, Yang P, Sun Y, Wu Y, Mayers B, Gates B, Yin Y, Kim F, Yan H. One-dimensional nanostructures: synthesis, characterization, and applications. *Advanced Materials* 2003; **15**(5):353–389.
9. Craighead HG. Nanoelectromechanical systems. *Science* 2000; **290**:1532–1535.
10. Lavrik NV, Sepaniak MJ, Datskos PG. Cantilever transducers as a platform for chemical and biological sensors. *Review of Scientific Instruments* 2004; **75**(7):2229–2253.
11. Ekinci KL, Roukes ML. Nanoelectromechanical systems. *Review of Scientific Instruments* 2005; **76**:061101.
12. Sun CQ, Tay BK, Zeng XT, Li S, Chen TP, Zhou J, Bai HL, Jiang EY. Bond-order-bond-length-bond-strength (bond-OLS) correlation mechanism for the shape-and-size dependence of a nanosolid. *Journal of Physics: Condensed Matter* 2002; **14**:7781–7795.
13. Cammarata RC. Surface and interface stress effects in thin films. *Progress in Surface Science* 1994; **46**(1):1–38.
14. Diao J, Gall K, Dunn ML. Surface-stress-induced phase transformation in metal nanowires. *Nature Materials* 2003; **2**(10):656–660.
15. Park HS, Gall K, Zimmerman JA. Shape memory and pseudoelasticity in metal nanowires. *Physical Review Letters* 2005; **95**:255504.
16. Liang W, Zhou M, Ke F. Shape memory effect in Cu nanowires. *Nano Letters* 2005; **5**(10):2039–2043.
17. Park HS. Stress-induced martensitic phase transformation in intermetallic nickel aluminum nanowires. *Nano Letters* 2006; **6**(5):958–962.
18. Kondo Y, Takayanagi K. Gold nanobridge stabilized by surface structure. *Physical Review Letters* 1997; **79**(18):3455–3458.

19. Kondo Y, Ru Q, Takayanagi K. Thickness induced structural phase transition of gold nanofilm. *Physical Review Letters* 1999; **82**(4):751–754.
20. Jing GY, Duan HL, Sun XM, Zhang ZS, Xu J, Li YD, Wang JX, Yu DP. Surface effects on elastic properties of silver nanowires: contact atomic-force microscopy. *Physical Review B* 2006; **73**:235409.
21. Zhou LG, Huang H. Are surfaces elastically softer or stiffer? *Applied Physics Letters* 2004; **84**(11):1940–1942.
22. Shenoy VB. Atomistic calculations of elastic properties of metallic FCC crystal surfaces. *Physical Review B* 2005; **71**:094104.
23. Liang H, Upmanyu M, Huang H. Size-dependent elasticity of nanowires: nonlinear effects. *Physical Review B* 2005; **71**:241403(R).
24. Chen CQ, Shi Y, Zhang YS, Zhu J, Yan YJ. Size dependence of the Young's modulus of ZnO nanowires. *Physical Review Letters* 2006; **96**:075505.
25. Agrawal R, Peng B, Gdoutos E, Espinosa HD. Elasticity size effects in ZnO nanowires—a combined experimental-computational approach. *Nano Letters* 2008; **8**(11):3668–3674.
26. Li X, Ono T, Wang Y, Esashi M. Ultrathin single-crystalline-silicon cantilever resonators: fabrication technology and significant specimen size effect on Young's modulus. *Applied Physics Letters* 2003; **83**(15):3081–3083.
27. Park HS, Gall K, Zimmerman JA. Deformation of FCC nanowires by twinning and slip. *Journal of the Mechanics and Physics of Solids* 2006; **54**(9):1862–1881.
28. Han X, Zheng K, Zhang YF, Zhang X, Zhang ZL. Low-temperature in situ large-strain plasticity of silicon nanowires. *Advanced Materials* 2007; **19**:2112–2118.
29. Kizuka T, Takatani Y, Asaka K, Yoshizaki R. Measurements of the atomistic mechanics of single crystalline silicon wires of nanometer width. *Physical Review B* 2005; **72**:035333.
30. Haile JM. *Molecular Dynamics Simulations*. Wiley: New York, 1992.
31. Ji C, Park HS. Characterizing the elasticity of hollow metal nanowires. *Nanotechnology* 2007; **18**:115707.
32. McDowell MT, Leach AM, Gall K. Bending and tensile deformation of metallic nanowires. *Modelling and Simulation in Materials Science and Engineering* 2008; **16**:045003.
33. Diao J, Gall K, Dunn ML. Atomistic simulation of the structure and elastic properties of gold nanowires. *Journal of the Mechanics and Physics of Solids* 2004; **52**:1935–1962.
34. Lee B, Rudd RE. First-principles calculation of mechanical properties of Si (001) nanowires and comparison to nanomechanical theory. *Physical Review B* 2007; **75**:195328.
35. Kang K, Cai W. Brittle and ductile fracture of semiconductor nanowires—molecular dynamics simulations. *Philosophical Magazine* 2007; **87**(14–15):2169–2189.
36. Belytschko T, Liu WK, Moran B. *Nonlinear Finite Elements for Continua and Structures*. Wiley: New York, 2002.
37. Liu WK, Karpov EG, Zhang S, Park HS. An introduction to computational nano mechanics and materials. *Computer Methods in Applied Mechanics and Engineering* 2004; **193**:1529–1578.
38. Curtin WA, Miller RE. Atomistic/continuum coupling in computational materials science. *Modelling and Simulation in Materials Science and Engineering* 2003; **11**:R33–R68.
39. Liu WK, Karpov EG, Park HS. *Nano Mechanics and Materials: Theory, Multiscale Methods and Applications*. Wiley: New York, 2006.
40. Shilkrot LE, Miller RE, Curtin WA. Multiscale plasticity modeling: coupled atomistics and discrete dislocation mechanics. *Journal of the Mechanics and Physics of Solids* 2004; **52**:755–787.
41. Qian D, Wagner GJ, Liu WK. A multiscale projection method for the analysis of carbon nanotubes. *Computer Methods in Applied Mechanics and Engineering* 2004; **193**:1603–1632.
42. Oden JT, Prudhomme S, Romkes A, Bauman PT. Multiscale modeling of physical phenomena: adaptive control of models. *SIAM Journal on Scientific Computing* 2006; **28**(6):2359–2389.
43. Abraham FF, Broughton J, Bernstein N, Kaxiras E. Spanning the continuum to quantum length scales in a dynamic simulation of brittle fracture. *Europhysics Letters* 1998; **44**:783–787.
44. Rudd RE, Broughton JQ. Coarse-grained molecular dynamics and the atomic limit of finite elements. *Physical Review B* 1998; **58**:5893–5896.
45. E W, Huang ZY. A dynamic atomistic–continuum method for the simulation of crystalline materials. *Journal of Computational Physics* 2002; **182**:234–261.
46. Wagner GJ, Liu WK. Coupling of atomistic and continuum simulations using a bridging scale decomposition. *Journal of Computational Physics* 2003; **190**:249–274.
47. Park HS, Karpov EG, Liu WK, Klein PA. The bridging scale for two-dimensional atomistic/continuum coupling. *Philosophical Magazine* 2005; **85**(1):79–113.

48. Xiao SP, Belytschko T. A bridging domain method for coupling continua with molecular dynamics. *Computer Methods in Applied Mechanics and Engineering* 2004; **193**:1645–1669.
49. Fish J, Chen W. Discrete-to-continuum bridging based on multigrid principles. *Computer Methods in Applied Mechanics and Engineering* 2004; **193**:1693–1711.
50. Tadmor E, Ortiz M, Phillips R. Quasicontinuum analysis of defects in solids. *Philosophical Magazine A* 1996; **73**:1529–1563.
51. Arroyo M, Belytschko T. An atomistic-based finite deformation membrane for single layer crystalline films. *Journal of the Mechanics and Physics of Solids* 2002; **50**:1941–1977.
52. Zhang P, Huang Y, Geubelle PH, Klein PA, Hwang KC. The elastic modulus of single-wall carbon nanotubes: a continuum analysis incorporating interatomic potentials. *International Journal of Solids and Structures* 2002; **39**:3893–3906.
53. Park HS, Klein PA, Wagner GJ. A surface Cauchy–Born model for nanoscale materials. *International Journal for Numerical Methods in Engineering* 2006; **68**:1072–1095.
54. Park HS, Klein PA. Surface Cauchy–Born analysis of surface stress effects on metallic nanowires. *Physical Review B* 2007; **75**:085408.
55. Park HS, Klein PA. A surface Cauchy–Born model for silicon nanostructures. *Computer Methods in Applied Mechanics and Engineering* 2008; **197**:3249–3260.
56. Klein PA, Zimmerman JA. Coupled atomistic–continuum simulation using arbitrary overlapping domains. *Journal of Computational Physics* 2006; **213**:86–116.
57. Li X, E W. Multiscale modeling of the dynamics of solids at finite temperature. *Journal of the Mechanics and Physics of Solids* 2005; **53**:1650–1685.
58. Zhu T, Li J, Samanta A, Leach A, Gall K. Temperature and strain-rate dependence of surface dislocation nucleation. *Physical Review Letters* 2008; **100**:025502.
59. Yvonnet J, Quang HL, He Q-C. An XFEM/level set approach to modelling surface/interface effects and to computing the size-dependent effective properties of nanocomposites. *Computational Mechanics* 2008; **42**:119–131.
60. Wei G, Shouwen Y, Ganyun H. Finite element characterization of the size-dependent mechanical behaviour in nanosystems. *Nanotechnology* 2006; **17**:1118–1122.
61. She H, Wang B. A geometrically nonlinear finite element model of nanomaterials with consideration of surface effects. *Finite Elements in Analysis and Design* 2009; **45**:463–467.
62. He J, Lilley CM. The finite element absolute nodal coordinate formulation incorporated with surface stress effect to model elastic bending nanowires in large deformation. *Computational Mechanics* 2009; **44**:395–403.
63. Park HS, Klein PA. Surface stress effects on the resonant properties of metal nanowires: the importance of finite deformation kinematics and the impact of the residual surface stress. *Journal of the Mechanics and Physics of Solids* 2008; **56**:3144–3166.
64. Yun G, Park HS. Surface stress effects on the bending properties of fcc metal nanowires. *Physical Review B* 2009; **79**:195–421.
65. Park HS. Surface stress effects on the resonant properties of silicon nanowires. *Journal of Applied Physics* 2008; **103**:123–504.
66. Park HS. Quantifying the size-dependent effect of the residual surface stress on the resonant frequencies of silicon nanowires if finite deformation kinematics are considered. *Nanotechnology* 2009; **20**:115701.
67. Yun G, Park HS. A multiscale, finite deformation formulation for surface stress effects on the coupled thermomechanical behavior of nanomaterials. *Computer Methods in Applied Mechanics and Engineering* 2008; **197**:3337–3350.
68. Tang Z, Zhao H, Li G, Aluru NR. Finite-temperature quasicontinuum method for multiscale analysis of silicon nanostructures. *Physical Review B* 2006; **74**:064110.
69. Huang WJ, Sun R, Tao J, Menard LD, Nuzzo RG, Zuo JM. Coordination-dependent surface atomic contraction in nanocrystals revealed by coherent diffraction. *Nature Materials* 2008; **7**:308–313.
70. Klein PA. A virtual internal bond approach to modeling crack nucleation and growth. *Ph.D. Thesis*, Stanford University, 1999.
71. Foiles SM, Baskes MI, Daw MS. Embedded-atom-method functions for the FCC metals Cu, Ag, Au, Ni, Pd, Pt, and their alloys. *Physical Review B* 1986; **33**(12):7983–7991.
72. Tersoff J. Modeling solid-state chemistry: interatomic potentials for multicomponent systems. *Physical Review B* 1989; **39**(8):5566–5568.
73. Tahoe. Available from: <http://tahoe.ca.sandia.gov>.

74. Wu X-F, Dzenis YA. Wave propagation in nanofibers. *Journal of Applied Physics* 2006; **100**:124318.
75. Song F, Huang GL, Varadan VK. Study of wave propagation in nanowires with surface effects by using a high-order continuum theory. *Acta Mechanica* 2010; **209**:129–139.
76. Wan J, Fan YL, Gong DW, Shen SG, Fan XQ. Surface relaxation and stress of FCC metals: Cu, Ag, Au, Ni, Pd, Pt, Al and Pb. *Modelling and Simulation in Materials Science and Engineering* 1999; **7**:189–206.
77. Balamane H, Halicioglu T, Tiller WA. Comparative study of silicon empirical interatomic potentials. *Physical Review B* 1992; **46**(4):2250–2279.
78. Wang L, Hu H. Flexural wave propagation in single-walled carbon nanotubes. *Physical Review B* 2005; **71**:195412.